

Dynamical Formation and Stability of Helical Prominence Magnetic Fields

C. Richard DeVore

Laboratory for Computational Physics and Fluid Dynamics, Naval Research Laboratory,
Washington, DC, 20375-5344; devore@nrl.navy.mil

and

Spiro K. Antiochos

E. O. Hulbert Center for Space Research, Naval Research Laboratory,
Washington, DC, 20375-5352; antiochos@nrl.navy.mil

Received _____; accepted _____

ABSTRACT

We numerically simulated an initially bipolar magnetic field subjected to shear motions concentrated near and parallel to the photospheric polarity inversion line. The simulations yield three principal results: (1) For footpoint displacements comparable to the bipole's depth, the sheared core field acquires a dipped geometry that can support cool prominence material against gravity. This confirms previous force-free equilibrium models for forming dipped prominence fields by differential shear, and extends them to much larger applied shears and time-dependent dynamics with dissipation. (2) At larger shears, we discover a new mechanism for forming the helical magnetic fields of prominences. It entails a two-step process of magnetic reconnection in the corona. First, flux in the sheared core reconnects with flux in the unsheared, restraining arcade, producing new pairs of interlinked field lines. Second, as these interlinked fields continue to be sheared, they are brought together and reconnect again, producing helical field threading and enveloping the body of the prominence. This mechanism can account for the twist that is often observed in both quiescent and erupting prominences. (3) Even for very large shears, the dipped, helical structure settles into an apparently stable equilibrium, despite the substantial amount of reconnection and twist in the magnetic field. We conclude that neither a kink instability of the helical core field, nor a tether-cutting instability of the restraining arcade, is operating in our low-lying model prominence. This concurs with both observations and a theoretical model for prominence stability.

Subject headings: Sun: activity — Sun: magnetic fields — Sun: prominences

1. INTRODUCTION

Prominences are perhaps the most beautiful and dramatic manifestations of magnetic structure and activity on the Sun. Observed in emission as prominences at the limb, and in absorption as filaments against the disk, these objects appear as columns or sheets of cold, dense plasma suspended above the solar surface. The fascination of prominences, together with their role as a crucially important component of solar activity, has spawned much effort to understand their physics (e.g., Tandberg-Hanssen 1974; Priest 1988a; Ruzdjak & Tandberg-Hanssen 1990; Tandberg-Hanssen 1995; Webb, Rust, & Schmieder 1998).

Our focus in this paper will be the magnetic field of prominences and its dynamics. Several ubiquitous features of the prominence magnetic environment have been identified (for recent reviews, see Demoulin 1998; Martin 1998a). Filaments always form above, and roughly aligned with, a polarity inversion line of the underlying photospheric field. The region between the photosphere and filament is a corridor or channel largely devoid of vertical field, but with H α fibrils lying parallel to the inversion line, suggesting a very strongly sheared magnetic field. Overlying the filament is an arcade crossing the inversion line at more nearly right angles, and so comprised of essentially current-free field. Within the prominence plasma itself, the horizontal field component orthogonal to the polarity inversion line of the underlying photospheric field usually points from the negative to the positive polarity side, in the opposite direction to a simple, potential arcade. That is, the prominence is said to exhibit inverse magnetic polarity (Leroy, Bommier, & Sahal-Bréchot 1984).

Two other features of the magnetic fields of prominences are difficult to measure directly, but have been inferred from plasma observations. One is a dipped, or concave-up, configuration of the internal field (Kippenhahn & Schlüter 1957; Kuperus & Raadu 1974). This is required to provide mechanical support to the plasma against gravity, in the form

of magnetic tension forces. Otherwise, the dense material would simply drain down to the photosphere, rather than being suspended in the corona. The second feature is helically coiled field within the prominence. Such structure has been observed in both quiescent and eruptive prominences (Vrsnak et al. 1988; Vrsnak, Ruzdjak, & Rompolt 1991; Martens 1998; Dere et al. 1999). Helical field lines threading the body of the prominence have dips, capable of supporting the plasma against gravity, at the bottom of each winding.

Global patterns exhibiting a handedness, or chirality, in the properties of filaments and their associated channels and arcades also have been revealed (Martin 1998b). Two classes of filaments exist: those in which the axial magnetic field points to the right when viewed from the positive-polarity side of the inversion line, called dextral, and those in which the axial field points to the left, called sinistral (Martin, Bilimoria, & Tracadas 1994). The skewed coronal arcades overlying filaments and filament channels also consistently take on one of two corresponding orientations: left-skewed, if the loops follow the threads of a left-handed screw, and right-skewed, otherwise (Martin & McAllister 1997). The skew decreases, and so the arcade field becomes more nearly perpendicular to the inversion line, with increasing height above the surface. Left-skewed arcades are associated with dextral filaments and channels, and right-skewed arcades with sinistral filaments and channels (Martin 1998b). Thus, the axial components of the filament, channel, and arcade fields are all aligned with each other.

A large number of models for the equilibrium magnetic fields of prominences have been proposed and studied. The paradigmatic models are those of Kippenhahn & Schlüter (1957), which features a nominally straight field with dips, producing a normal-polarity prominence, and of Kuperus & Raadu (1974), which contains a detached, closed flux bubble in the corona, and produces an inverse-polarity prominence. More recent work includes extensions of Kippenhahn-Schlüter configurations to encompass force-free fields with dips

and inverse polarity (Demoulin & Priest 1993; Antiochos, Dahlburg, & Klimchuk 1994; Aulanier & Demoulin 1998; Mackay, Longbottom, & Priest 1999), and of Kuperus-Raadu models containing helical fluxropes (Priest, Hood, & Anzer 1989; Low 1993; Hundhausen & Low 1994; Low & Hundhausen 1995; Rust & Kumar 1994, 1996). Two mechanisms for generating the helical fields in prominences have been suggested. One is a simple twisting of the fluxtube, due to flows in the convective zone prior to emergence through the photosphere (Low 1994, 1996; Rust & Kumar 1994, 1996) or to photospheric circulations acting on a fully emerged field (Amari et al. 1999). The second is reconnection of sheared magnetic field, in which pairs of sheared, but possibly untwisted, fluxtubes reconnect to form pairs of helical ropes (van Ballegooijen & Martens 1989, 1990; Ridgway & Priest 1993; Kuperus 1996; Priest, van Ballegooijen, & MacKay 1996; Galsgaard & Longbottom 1999; Amari et al. 1999). All of these latter models rely on converging motions of the photospheric flux toward the polarity inversion line, where the reconnection takes place.

The problems of prominence stability and the transition to eruptive behavior also have received a considerable amount of attention. Here again, two principal classes of models have been proposed and developed. The first is the onset of a magnetohydrodynamic instability. Ideal kink instabilities convulsing an increasingly twisted magnetic field (e.g., Raadu 1972; Hood & Priest 1979; Einaudi & Van Hoven 1983) have been discussed as a mechanism for prominence eruptions (Rust & Kumar 1994, 1996; Xu & Wu 1995). The mechanical instability of a current-carrying loop in MHD equilibrium (Vrsnak 1990) yields threshold criteria for eruptive behavior that agree well with prominence observations (Vrsnak et al. 1988, 1991). The second class of models is that of ‘loss of equilibrium,’ in which the evolution of the prominence eventually moves it into a regime where no equilibrium is accessible, leading to a rapid expulsion of the structure (Priest 1988b; Steele & Priest 1989). In either case, a mechanism to remove the overlying arcade fields, thereby allowing the prominence to escape from below, is required. One possibility is the ‘tether-cutting’

model, in which the stressed field rises and increasingly strains the magnetic tethers holding it down, eventually reconnecting them below and exploding outwards (Sturrock 1989, 1992; Moore & Roumeliotis 1992). This process can take place in a simple, bipolar magnetic structure. Another is the ‘break-out’ model, in which the restraining arcade reconnects in the corona with an overlying arcade from a distinct flux system, thereby moving the tethering field out of the way and allowing the prominence to escape from below (Antiochos, DeVore, & Klimchuk 1999). This process can occur only in a multipolar magnetic structure.

In this paper, we revisit the model proposed by Antiochos et al. (1994; hereafter ADK) for dipped magnetic equilibria capable of supporting prominence plasma. The parameter space they were able to investigate was limited by the numerical techniques used to obtain their force-free equilibria. Our approach is to use a time-dependent magnetohydrodynamic (MHD) model to simulate a possible dynamical scenario for prominence formation. For relatively modest deviations from an initially potential field, we recover the results of ADK: a dipped, sinuous magnetic structure exhibiting inverse polarity above the photospheric inversion line and below an arcade of essentially current-free field. At larger displacements, a two-step reconnection process is initiated which creates helical field wrapped around the dipped core of the prominence, and also skews the overlying arcade adjacent to the prominence. The resulting structure attains an apparently stable equilibrium, with substantial twist on some of its field lines. We show that our model prominence, scaled to solar parameters, has properties similar to those observed (Vrsnak et al. 1988). Its stability also accords with Vrsnak’s (1990) model for force balance in prominences, which predicts that low-lying structures are stable even if highly twisted, while taller structures are increasingly vulnerable to eruption.

2. MODEL

The model proposed by ADK requires a fully three-dimensional magnetic field configuration, but is intuitively quite simple. They began with a bipolar potential field, and subjected the footpoints to linear shearing displacements parallel to the polarity inversion line of the vertical field. These displacements were localized near the inversion line and changed sign across it. The initial field and the pattern of footpoint motions are illustrated in the left panels of Plate 1. As the sheared core flux was transported into regions of increasingly weak background field, it began to inflate upwards and eventually to lean over, across the polarity inversion line. The middle sections of these sheared field lines, on the other hand, were restrained from rising by the tension in the overlying, unsheared arcade. When the sheared flux had been displaced sufficiently, dipped field lines formed in the core. Because the legs at each end of the dipped lines leaned across the inversion line, the dipped portions of the field crossed the inversion line in the opposite direction from a simple, current-free arcade. That is, the transverse field within the prominence exhibited inverse polarity. The triple crossing of the inversion line also causes each dipped field line to assume an *S* or inverse-*S* shape. These features are illustrated in the right panels of Plate 1.

The magnetic and morphological properties of ADK's model prominence are all consistent with the observations cited earlier: a channel beneath the prominence that is essentially devoid of vertical flux; a nearly axial magnetic field whose horizontal component perpendicular to the inversion line has inverse polarity; a volume of dipped field to support condensed plasma against gravity; a sinuous morphology to the filament volume; and an overlying, approximately current-free arcade of coronal loops.

One ubiquitous feature of solar prominences not reproduced by their model was the presence of helical lines of force. As we shall see below, this was due solely to the limited parameter space that they were able to explore. ADK applied a relaxation technique

for force-free fields to the Euler potentials representing their magnetic flux distribution (Yang, Sturrock, & Antiochos 1986). At large displacements, however, the contours of the potentials become so distorted that it is impossible to resolve them adequately and iterate the solution to convergence on any reasonable spatial grid, and the simulation breaks down.

To simulate numerically the further development of the prominence magnetic field, we used our new, time-dependent, three-dimensional magnetohydrodynamics code *FCTMHD3D*. It is a three-dimensional (*3D*) extension of our previous MHD models, and employs similar flux-corrected transport (*FCT*) techniques (DeVore 1991) to advance the equations in time. *FCTMHD3D* was implemented on massively parallel computers to permit its use in lengthy simulations on well-resolved grids. Although the accuracy of our solutions is sensitive to the mesh size assumed, the model will not fail as increasingly fine-scale structure develops. Consequently, we have been able to extend the earlier results of ADK to much larger shearing displacements.

Our model solves the time-dependent, ideal MHD equations appropriate for the solar corona:

$$\frac{\partial \rho}{\partial t} + \nabla \cdot (\rho \mathbf{v}) = 0, \quad (1)$$

$$\frac{\partial \rho \mathbf{v}}{\partial t} + \nabla \cdot (\rho \mathbf{v} \mathbf{v}) = -\nabla P + \frac{1}{4\pi}(\nabla \times \mathbf{B}) \times \mathbf{B}, \quad (2)$$

$$\frac{\partial U}{\partial t} + \nabla \cdot (U \mathbf{v}) = -P \nabla \cdot \mathbf{v}, \quad (3)$$

$$\frac{\partial \mathbf{B}}{\partial t} = \nabla \times (\mathbf{v} \times \mathbf{B}), \quad (4)$$

where ρ is the mass density, \mathbf{v} is the velocity, P is the gas pressure, \mathbf{B} is the magnetic field, and U is the internal energy density, $U = P/(\gamma - 1) = 3P/2$. Although no explicit electrical resistivity is included in the model, a finite amount of grid- and solution-dependent dissipation is introduced by our numerical algorithm. This dissipation, which is common to all stable integration schemes for the induction equation, is small but sufficient to allow the magnetic field to reconnect, as will be seen below.

We are concerned here only with the development of the magnetic structure in the low-beta corona, where the atmospheric scale height is large. Thus, we have omitted gravity from the model. Furthermore, the ideal MHD equations can be made dimensionless by scaling out a mass density ρ_0 , field strength B_0 , and region size L , and appropriate combinations of those parameters for other quantities such as velocity ($B_0/\rho_0^{1/2}$) and energy ($B_0^2 L^3$). We used this freedom to set the initially uniform mass density, the characteristic length, and the peak Alfvén speed of our initial state to numbers of order unity, for computational convenience.

A useful diagnostic of the calculations is the magnetic helicity,

$$H_M = \int dV \mathbf{A} \cdot \mathbf{B}, \quad (5)$$

where \mathbf{A} is the vector potential,

$$\mathbf{B} = \nabla \times \mathbf{A}, \quad (6)$$

and the integral is evaluated over the entire coronal volume. The helicity must be made gauge-invariant, and thereby unique, by subtracting off the helicity of a current-free field with the same distribution of vertical magnetic flux at the coronal base (Berger & Field 1984). If the vector potential \mathbf{A}_c for that current-free field satisfies the Coulomb gauge condition ($\nabla \cdot \mathbf{A}_c = 0$) and has a vanishing normal component at the base ($\hat{\mathbf{n}} \cdot \mathbf{A}_c|_S = 0$), then the potential helicity integral vanishes and we are left with the given expression for H_M . A suitable \mathbf{A}_c can be constructed immediately from the corresponding scalar potential, ϕ_c , for the current-free field. In cartesian geometry (x, y, z) , where z is the height above the bounding coronal surface, we take

$$\mathbf{A}_c(x, y, z) = \nabla \times \hat{\mathbf{z}} \int_z^\infty dz' \phi_c(x, y, z'). \quad (7)$$

From this definition and $\nabla^2 \phi_c = 0$ it follows readily (see the Appendix) that

$$\nabla \times \mathbf{A}_c = -\nabla \phi_c, \quad (8)$$

i.e., the magnetic fields produced by these scalar and vector potentials are identical. The scalar potential ϕ_c is evaluated as an integral over the vertical flux distribution at the base, using Green's function for Laplace's equation as the integration kernel,

$$\phi_c(x, y, z) = \frac{1}{2\pi} \int \int dx' dy' \frac{B_z(x', y', 0)}{\left[(x - x')^2 + (y - y')^2 + z^2 \right]^{1/2}}. \quad (9)$$

This result is used in turn to calculate the vector potential \mathbf{A}_c at the base, $z = 0$. Finally, these boundary values are used to compute the vector potential \mathbf{A} for the actual magnetic field \mathbf{B} , by integration:

$$\mathbf{A}(x, y, z) = \mathbf{A}_c(x, y, 0) - \hat{\mathbf{z}} \times \int_0^z dz' \mathbf{B}(x, y, z'). \quad (10)$$

The helicity integral H_M is then performed, completing the calculation.

3. RESULTS

The simulations described here were performed for an initial field comprised of a horizontal point dipole oriented along the y axis, at depth $d = 2$ and characteristic strength $\bar{B} = 4$, whose scalar potential can be written

$$\phi(x, y, z) = \bar{B}d^3 \frac{y}{[x^2 + y^2 + (z + d)^2]^{3/2}}. \quad (11)$$

In the half-space $z \geq 0$, the resulting field reaches its maximum magnitude B_{\max} at $x = z = 0, y = \pm d/2 = \pm 1$, where $B_{\max} \approx |\bar{B}| = 4$. The peak Alfvén speed for unit mass density is $B_{\max}/(4\pi\rho)^{1/2} \approx (4/\pi)^{1/2} = 1.13$. A uniform pressure of 1×10^{-2} was assumed, so the minimum plasma $\beta = 8\pi P/B_{\max}^2$ was 1.6×10^{-2} . Contours of B_z at the base plane $z = 0$ and a few selected field lines for the initial state were shown in the left panel of Plate 1. Also shown were velocity vectors representing the imposed footpoint motions. The corresponding displacements have $\delta y = 0$ and

$$\delta x = \delta x_{\max} f(t) \times \begin{cases} \sin(\pi y/w), & |y| \leq w; \\ 0, & |y| > w. \end{cases} \quad (12)$$

A smooth, sinusoidal acceleration and deceleration was imposed using the temporal profile

$$f(t) = \frac{t}{\tau} - \frac{1}{2\pi} \sin\left(2\pi\frac{t}{\tau}\right). \quad (13)$$

The associated peak footpoint speed, $2\delta x_{\max}/\tau$, is attained at $y = \pm w/2$ and $t = \tau/2$. We used $w = d/2 = 1$, so that the displacement vanished at and beyond the location of peak field strength, as shown in Plate 1. Consequently, 20% of the total flux in the dipole was subjected to footpoint motions of finite amplitude.

Open boundary conditions, with zero-gradient extrapolations of all variables, were used on the four sides and the top of the domain. At the base plane, we held the mass density ρ and pressure P fixed at their initial values, set the horizontal velocities to correspond to the footpoint displacements prescribed above, and required the vertical velocity to vanish, $v_z = 0$. The horizontal magnetic field at the base was extrapolated assuming zero gradient, as was done at the remaining five boundaries, and the vertical magnetic field evolved in response to the imposed footpoint motions.

Our computational domain extended over $[-24, +24]$ in x , $[-6, +6]$ in y , and $[0, 12]$ in z . The nonuniform grid was stretched exponentially away from the origin, in all three directions, from cubic cells of size 2.4×10^{-2} . The cells were stretched by a factor of 10 along x and by a factor of 5.5 along y and z . About one-third of the grid points lay within $[-3, +3]$ in x , $[-1, +1]$ in y , and $[0, 2]$ in z . The full grid for these simulations was $500 \times 190 \times 190$.

For comparison with the earlier results of ADK, we applied a rather modest shear to the initial field. We began with a maximum displacement $\delta x_{\max} = 4$ applied over a time $\tau = 25$, then allowed the field to relax until time $t = 70$. We next applied an additional shear $\delta x_{\max} = 2$ over time $\tau = 12.5$, and allowed the field to relax again, until time $t = 120$. The results were shown in the right panel of Plate 1. We recovered all of the principal qualitative features noted in the earlier work of ADK. The core field lines in the sheared region have developed dipped central sections, where they are restrained from rising by

the overlying, nearly potential-field arcade. The end sections of these sheared lines, on the other hand, have ballooned upwards substantially where the overlying coronal field is weak. They also have leaned across the polarity inversion line of the photospheric field below, into regions of weaker coronal field. As a consequence, the dipped lines have a significant field component transverse to the inversion line, which points from the negative side to the positive side. Thus, the transverse field exhibits inverse polarity, relative to that expected in a current-free arcade. Finally, the leaning of the strongly sheared field across the inversion line produces a triple crossing by the dipped field lines. This lends an *S* or inverse-*S* shaped morphology to the core field of the filament, as is frequently observed.

Our model prominence is of the dextral type, since its axial field points to the right when viewed from the positive polarity side of the flux distribution (Martin et al. 1994). Repeating the experiment with the sign of the footpoint displacements reversed would produce the mirror image of our results, i.e., a sinistral prominence.

To examine the properties of more strongly sheared fields, we repeated the simulation with a maximum displacement $\delta x_{\max} = 16$ applied over a time $\tau = 100$, both larger by factors of four than previously. The associated peak footpoint speed was unchanged. We found that an intricate, two-step process of magnetic reconnection takes place in the sheared, dipped field of the prominence. This sequence is illustrated in Plates 2 and 3.

Illustrative field lines of the configuration at time $t = 55$ are shown in Plate 2. At this point, the peak displacement has reached 60% of its final value, or 9.6, compared to a total peak displacement of 6 in our ADK comparison shown earlier. Overhead (upper panels) and perspective (lower panels) views are given of two complementary sets of magnetic field lines. Pre-reconnection field lines are shown in light and dark blue in the left panels. The light blue lines are strongly sheared field originating near the edges of the vertical flux distribution, while the dark blue lines are part of the overlying arcade, on the outside edge

of the region of sheared flux. Also shown is a dark gray line in the core of the sheared flux, along with isosurfaces of the electric current density at 75% of peak strength, in black. The currents are strongest along the inside edges of the dark blue arcade field lines, where the light blue sheared lines have leaned over across the inversion line sufficiently to come into contact and reconnect with the unsheared dark blue lines.

Post-reconnection field lines are shown in light and dark red and green in the right panels of Plate 2. The red lines result from reconnection between the light and dark blue pair of lines on the far side of the inversion line, as seen in the left panels; the green lines form from the light and dark blue pair on the near side. The reconnected lines lie farther out along the direction of footpoint displacement, toward the ends of the vertical flux distribution, where the reconnection is initiated. With time, the location of strong currents and reconnection migrates across the inner face of the arcade. Relaxation of the tension in the reconnected field lines largely eliminates the dips present in the pre-reconnection field, as is evident in the lower right panel. The light shaded, post-reconnection field lines take the form of simple, sheared loops with normal transverse polarity above the photospheric inversion line. The dark shaded red and green lines loop over the inversion line with normal polarity near the ends of the vertical flux distribution, beginning from the arcade’s inner edge, then stretch well into the region of sheared flux on the far side. In so doing, these lines thread under and through each other, resembling linked shepherd’s crooks when viewed from above, as in the upper right panel. Inspection of this configuration suggests that after further displacement, the dark red and green lines will be dragged into contact with each other and reconnect again. This is precisely what happens in step two of the reconnection process.

Pre- and post-reconnection field lines at time $t = 75$ are shown in the left and right panels, respectively, of Plate 3. The peak displacement now has reached 91% of its final

value, or 14.5. Dark red and green lines of pre-reconnection field in the left panel are similar to those lines that were produced in step one of the process, and shown in the right panel of Plate 2. Those shown in Plate 3 were formed later and, thus, nearer the symmetry line of the original bipole. A very strongly dipped and sheared core field line of the structure is again shown in dark gray, and the isosurface of the electric current magnitude is drawn in black. The latter is now a very compact region at the contact point between the dark red and green lines, where they have been forced together by the ongoing displacement of the footpoints. Dips have reformed in these field lines as the shearing has continued, though with only weak components transverse to the inversion line. For completeness, the light red and green lines corresponding to those in Figure 2 also are shown, although they play no role in this second step of the reconnection process.

Post-reconnection field lines are shown in dark and light blue in the right panels of Plate 3. The overlying portions of the pre-reconnection fields produce a left-skewed coronal loop, in dark blue. It resides beneath the higher, potential-field arcade (not shown), whose field lines cross the polarity inversion line at right angles. Such left-skewed arcades seem invariably to be associated with dextral prominences (Martin & McAllister 1997), as is the case here. Reversing the sign of the footpoint displacement in our simulation would produce the mirror image of this plate, i.e., a sinistral prominence field with an overlying, right-skewed arcade.

The strongly sheared parts of the pre-reconnection fields form a new field line, in light blue, that wraps around the core of the dipped prominence field, represented by the dark gray line. A helical twist to the enveloping field line is suggested in Plate 3, but becomes clearer after the field has relaxed nearer to its equilibrium state. Plate 4 shows selected lines at time $t = 100$, when the footpoint displacement is stopped. The helical structure is now much more pronounced. From the footpoints, the field loops up and over the inversion

line below, then recrosses the line near the bottom of the winding. Consequently, at the bottoms of the helical windings the transverse field exhibits inverse polarity. The much shallower dip in the central section of the line, on the other hand, has a normal-polarity transverse field. Thus, the portions of the field capable of supporting prominence plasma are mainly inverse polarity, but have a small admixture of normal-polarity field.

Following the cessation of the imposed footpoint motions, we allowed the structure to relax for a time equal to the shearing time, i.e., to time $t = 200$. Further reconnections occurred in the field during this phase, producing additional helical structure but no qualitatively new features. The kinetic energy E_K of the system continued to decline monotonically from the peak reached at time $t = 65$, just past the halfway point of the shearing phase, to less than 25% of peak at $t = 200$. Both the magnetic energy E_M and helicity H_M were essentially flat throughout the relaxation. These results, appropriately normalized, are shown in Figure 1. The final magnetic energy was 235% of the initial value. That level was attained at about $t = 65$, when the kinetic energy also peaked. The magnetic helicity declined monotonically from zero to its final value of -0.97, reached at time $t = 100$ when the footpoint motion was stopped. The negative sign is consistent with the left-handed helices of the prominence field and the skew of the overlying arcade. Reversing the direction of the footpoint displacements would reverse the sign of the resultant magnetic helicity, along with the chirality of the prominence and arcade fields.

For comparison with some properties of observed prominences, we scaled our numerical results by a factor of 10 in field strength and 10^9 in length. This corresponds to an initial bipole with characteristic strength 40 G, pole separation 20 Mm, and 3.2×10^{20} Mx of magnetic flux. The dipped, helical field line shown in Plate 4 then has a flux density within the prominence of 20 G, and carries an electric current whose density is 1×10^{-4} A m $^{-2}$. This field line also exhibits two full turns from end to end, approximately, for a total twist

of 4π . It defines a quasi-cylindrical volume of radius 10 Mm, height 20 Mm, and length 250 Mm. Thus, the prominence carries a total current of a few times 10^{10} A. These parameters are commensurate with those of a sample of prominences analyzed by Vrsnak et al. (1988). The principal exception is that our model prominence is rather low-lying and elongated compared to the prominences included in their study, with a ratio of length to height (12.5) more than double their largest observed value (5). Our configuration is not extraordinary for the Sun, however, whose filaments can exceed 500 Mm in length at heights of about 40 Mm (e.g., Giovanelli 1984). About 1×10^{30} erg of magnetic energy and -2.5×10^{40} Mx² of magnetic helicity are contained in our model prominence.

4. DISCUSSION

The results of the numerical simulations described here confirm and significantly extend the earlier findings of Antiochos et al. (1994). Their study of force-free magnetic equilibria showed that dipped magnetic fields capable of supporting radiatively condensed plasma against gravity could be formed in modestly sheared bipolar configurations, in the presence of a sufficiently strong overlying coronal arcade. The arcade restrains the vertical rise of the midsections of the sheared field lines. In the weak-field regions beyond the arcade and adjacent to the polarity inversion line, on the other hand, the sheared flux is not so restrained and the field rises much higher. This produces the dipped configuration of the sheared field lines. Due to the absence of flux on the far side of the inversion line, the sheared field also leans over across the inversion line below. This has two effects: it produces a triple crossing of the inversion line by the dipped, prominence field from one footpoint to the other, and lends an inverse polarity to the horizontal component of the field, which points in the opposite direction to that of a simple, current-free arcade. Displacing the innermost flux of the bipole along the polarity inversion line, which eventually produces the

dipped structure, also leaves the photosphere below the prominence dips essentially devoid of vertical field. All of these properties are consistent with those of observed prominences (Demoulin 1998; Martin 1998a).

We now have demonstrated that the application of greater shear eventually drives reconnection in the corona, between the highly stressed core flux of the prominence and the overlying, unsheared arcade. The most important consequence of this reconnection is the production of helical field lines threading the prominence and enveloping its core field. Such structure is ubiquitous in both pre-eruptive and eruptive prominences (Vrsnak et al. 1988, 1991; Martens 1998; Dere et al. 1999). The magnetic field at the bottom of the helical windings, where the plasma can be expected to condense, exhibits the same inverse polarity as does the dipped field at weaker shear. A second consequence of the reconnection process is the skewing of the overlying arcade. This seems to be a necessary consequence of the formation of the helical field in our model. However, a skewed arcade is not sufficient to establish that helical fields are present. By broadening and adding a slow dropoff to the imposed shear profile, we could always produce a skewed arcade over the dipped field of our model prominence.

The direction of the footpoint displacement applied in our simulations was such as to inject negative magnetic helicity into the coronal field and produce a dextral filament - the axial field of the prominence points to the right when viewed from the positive polarity side of the structure - and a left-skewed arcade. Reversing the footpoint displacement would yield the mirror image of the results shown here, i.e., a sinistral filament with a right-skewed arcade and positive magnetic helicity. The classification of filaments into dextral and sinistral types was proposed by Martin, Bilimoria, & Tracadas (1994), and the association of left- and right-skewed arcades, respectively, with these two types was discussed by Martin & McAllister (1997). Our model is in agreement with this observed association.

More recently, however, Martin (1998b) has suggested that the helicities of the filament and the overlying arcade are of opposite sign. Thus, the internal magnetic field of a dextral filament would be right-helical, rather than left-helical as in our model. Such a configuration is difficult to reconcile with correlated observations of disappearing filaments (*disparition brusques*) and interplanetary magnetic clouds (Bothmer & Schwenn 1994; Rust 1994; Bothmer & Rust 1997). This work has shown a strong and consistent association between dextral filaments and left-handed, negative-helicity clouds, principally originating in the Sun’s northern hemisphere, on the one hand, and between sinistral filaments and right-handed, positive-helicity clouds, mostly from the southern hemisphere, on the other. The absence of multiple reversals of the out-of-ecliptic magnetic field during passage suggests that the clouds are entirely left- or right-helical, but not mixed. Martin argues that the filament itself either was never entrained or was dissipated in transit, and the cloud field is a remnant of the enclosing coronal arcade only. Our results are consistent only with the simpler picture of like helicity in the arcade and the imbedded filament.

The negative magnetic helicity of dextral filaments, which predominate in the northern hemisphere, also is consistent with the demonstrated tendency for solar differential rotation to inject negative helicity into northern-hemisphere bipolar regions (van Ballegooijen 1999; DeVore 1999). Positive helicity is injected into bipolar regions in the southern hemisphere, where positive-helicity, sinistral filaments are more numerous. The shear required to produce our model prominence fields admittedly is much more concentrated near the polarity inversion line than is the Sun’s differential rotation, which is global in scale. However, there is observational evidence that active regions contain much more strongly sheared magnetic fields than differential rotation alone would produce (e.g., Schmieder et al. 1996). Certainly, such sheared configurations develop very frequently on the Sun, whatever their origin in footpoint motions and/or patterns of flux emergence.

Footpoint motions play a critical role in one class of models for forming helical magnetic fields in prominences (van Ballegooijen & Martens 1989, 1990; Ridgway & Priest 1993; Kuperus 1996; Priest et al. 1996; Galsgaard & Longbottom 1999; Amari et al. 1999). The convergence of sheared fields at the polarity inversion line, whether due to coherent flows or to the random shuffling of fluxtubes in the unsteady photospheric convection, produces helical structure when the fields reconnect. Our mechanism differs from these models in not requiring a convergence of flux at the photosphere, and in the reconnection process taking place in the corona. It is plausible that both mechanisms are at work simultaneously, producing helical prominence fields on the Sun.

Other models that attempt to account for helical structure in filaments rely on subsurface motions to twist the fluxtubes prior to emergence through the photosphere (Low, 1994, 1996; Rust & Kumar 1994, 1996) or on twisting surface motions after emergence (Amari et al. 1999). Such models clearly can explain certain observed properties of prominences. On the other hand, there seems to be sufficient freedom in these models to admit prominence-like configurations unlike those actually observed on the Sun. For example, although overlying arcades of current-free field can be accommodated by the models, there seems to be no essential need for them. In our scenario, in contrast, the overlying arcade is absolutely vital to the process, and the prominence cannot form without it. Secondly, consider the relation of the prominence to the underlying photospheric inversion line. A partially emerged, twisted fluxtube could have a fully emerged, helical core - the prominence itself - suspended above and parallel to the inversion line of the photospheric field, which consists of the flux cutting through a chordal plane of the tube cross section. This agrees with observations. When fully emerged, on the other hand, such a twisted fluxtube would have its helical core suspended above and lying orthogonal to the inversion line of the photospheric field, which now consists of the footpoints of the fluxtube field lines. This is in conflict with observations, but evidently allowed by the models. In our scenario,

the helical prominence can only extend nearly parallel to the photospheric inversion line, as observed. Thirdly, the helical fluxtube can be structured so as to exclude vertical field at the photosphere directly below the prominence. Clearly, however, it can just as easily include substantial vertical field there, which disagrees with observations. In our scenario, the prominence field is precisely the vertical field adjacent to the polarity inversion line, after it has been swept out from under the overlying arcade by the differential shear. Consequently, the photosphere under our model prominence is always essentially devoid of vertical field, in accord with observations.

We found that our model prominence settled into an evidently MHD-stable equilibrium after the footpoint displacements were stopped, despite the very large applied shear and the substantial internal helical structure. Furthermore, when scaled to typical solar parameters for field strength and size, the properties of our model prominence were largely consistent with those of observed prominences (Vrsnak et al. 1988). In particular, we found a twist of about 4π radians on our most twisted field lines, similar to those reported. These results seem to be incompatible with kink-instability models for eruptive prominences, in which about 2π of twist is sufficient to launch the instability, and presumably the eruption (Rust & Kumar 1994, 1996; Xu & Wu 1995). On the other hand, our results are fully consistent with Vrsnak's (1990) model for prominence equilibrium and stability. Low-lying structures are stable even for very large twists; taller structures are increasingly susceptible to eruption as the electric current, and twist, increase. A sizable sample of observed quiescent and eruptive prominences has been analyzed (Vrsnak et al. 1991) and found to agree well with the predictions of Vrsnak's model.

These considerations suggest that our simulated prominence may be stable because it is very long for its height, relative to those observed to be prone to eruption. The tether-cutting mechanism for prominence eruption (Sturrock 1989, 1992; Moore & Roumeliotis 1992)

predicts that such a highly stressed bipolar structure undergoing magnetic reconnection will begin to rise and eventually erupt as the stress builds and then exceeds some critical threshold. Although our prominence field is very highly stressed and clearly has undergone substantial reconnection, no significant cutting of its magnetic tethers has taken place, and the structure apparently is stable. To induce such cutting would require us to modify the boundary conditions at the coronal base, to produce converging flows of opposite-polarity fields at the polarity inversion line. Ideally, we would like to adjust our model parameters so as to produce a much taller prominence, more like those typically observed. This might be done by increasing the width of the imposed shear profile, and thus the fraction of flux that is being sheared, thereby lowering the fraction reserved for the overlying arcade. The challenge would be to retain sufficient flux in the arcade to produce the dips and helical windings in the core field, while simultaneously reducing it enough to allow the resulting prominence to rise substantially in height. This study, which could provide truly definitive tests of both the prominence instability theory and the tether-cutting mechanism for eruption, must be left to the future.

The development of *FCTMHD3D* was sponsored by NASA’s High Performance Computing and Communications program in Earth and Space Sciences, and the numerical simulations were performed using grants of time from the DoD’s High Performance Computing Modernization Program. This research also was supported by NASA and ONR programs in Solar Physics and the Sun-Earth Connection.

A. EQUIVALENCE OF SCALAR AND VECTOR POTENTIALS

To demonstrate the equivalence of the magnetic fields derived from a scalar potential ϕ_c and its associated Coulomb-gauge vector potential \mathbf{A}_c given by equation (7),

$$\mathbf{A}_c(x, y, z) = \nabla \times \hat{\mathbf{z}} \int_z^\infty dz' \phi_c(x, y, z'), \quad (\text{A1})$$

we first express the curl of this vector in the form

$$\nabla \times \mathbf{A}_c = \nabla \left(\nabla \cdot \hat{\mathbf{z}} \int_z^\infty dz' \phi_c(x, y, z') \right) - \nabla^2 \hat{\mathbf{z}} \int_z^\infty dz' \phi_c(x, y, z'). \quad (\text{A2})$$

The first term is

$$\nabla \left(\nabla \cdot \hat{\mathbf{z}} \int_z^\infty dz' \phi_c(x, y, z') \right) = -\nabla \phi_c, \quad (\text{A3})$$

and the second term vanishes, since $\nabla^2 \phi_c = 0$ and $\partial \phi_c / \partial z|_{z \rightarrow \infty} = 0$ give

$$\begin{aligned} \nabla^2 \int_z^\infty dz' \phi_c(x, y, z') &= \int_z^\infty dz' \left(\frac{\partial^2}{\partial x^2} + \frac{\partial^2}{\partial y^2} \right) \phi_c(x, y, z') + \frac{\partial^2}{\partial z^2} \int_z^\infty dz' \phi_c(x, y, z') \\ &= - \int_z^\infty dz' \frac{\partial^2}{\partial z'^2} \phi_c(x, y, z') - \frac{\partial \phi_c}{\partial z} \\ &= 0. \end{aligned} \quad (\text{A4})$$

Thus, as stated in equation (8),

$$\nabla \times \mathbf{A}_c = -\nabla \phi_c. \quad (\text{A5})$$

REFERENCES

- Amari, T., Luciani, J. F., Mikic, Z., & Linker, J. 1999, ApJ, 518, L57
- Antiochos, S. K., Dahlburg, R. B., & Klimchuk, J. A. 1994, ApJ, 420, L41
- Antiochos, S. K., DeVore, C. R., & Klimchuk, J. A. 1999, ApJ, 510, 485
- Aulanier, G., & Demoulin, P. 1998, A&A, 329, 1125
- Berger, M. A., & Field, G. B. 1984, J. Fluid Mech., 147, 133
- Bothmer, V., & Rust, D. M. 1997, in Coronal Mass Ejections, ed. Crooker, N., Joselyn, J. A., & Feynman, J. (Washington: American Geophysical Union), 139
- Bothmer, V., & Schwenn, R. 1994, Space Science Reviews, 70, 215
- Demoulin, P. 1998, in New Perspectives on Solar Prominences, ed. Webb, D., Rust, D., & Schmieder, B. (San Francisco: Astronomical Society of the Pacific), 78
- Demoulin, P., & Priest, E. R. 1993, Sol. Phys., 144, 283
- Dere, K. P., Brueckner, G. E., Howard, R. A., Michels, D. J., & Delaboudiniere, J. P. 1999, ApJ, 516, 465
- DeVore, C. R. 1991, J. Comp. Phys., 92, 142
- DeVore, C. R. 1999, ApJ, submitted
- Einaudi, G., & Van Hoven, G. 1983, Sol. Phys., 88, 163
- Galsgaard, K., & Longbottom, A. W. 1999, ApJ, 510, 444
- Giovanelli, R. G., 1984, Secrets of the Sun (Cambridge: Cambridge)
- Hood, A. W., & Priest, E. R. 1979, Sol. Phys., 64, 303

- Hundhausen, J. R., & Low, B. C. 1994, ApJ, 429, 876
- Kippenhahn, R., & Schlüter, A. 1957, Zeitschrift fur Astrophysik, 43, 36
- Kuperus, M. 1996, Sol. Phys., 169, 349
- Kuperus, M., & Raadu, M. A. 1974, A&A, 31, 189
- Leroy, J. L., Bommier, V., & Sahal-Bréchot, S. 1984, A&A, 131, 33
- Low, B. C. 1993, ApJ, 409, 798
- Low, B. C. 1994, Phys. Plasmas, 1, 1684
- Low, B. C. 1996, Sol. Phys., 167, 217
- Low, B. C., & Hundhausen, J. R. 1995, ApJ, 443, 818
- Mackay, D. H., Longbottom, A. W., & Priest, E. R. 1999, Sol. Phys., 185, 87
- Martens, P. C. H. 1998, in New Perspectives on Solar Prominences, ed. Webb, D., Rust, D., & Schmieder, B. (San Francisco: Astronomical Society of the Pacific), 294
- Martin, S. F. 1998a, Sol. Phys., 182, 107
- Martin, S. F. 1998b, in New Perspectives on Solar Prominences, ed. Webb, D., Rust, D., & Schmieder, B. (San Francisco: Astronomical Society of the Pacific), 419
- Martin, S. F., Bilimoria, R., & Tracadas, P. W. 1994, in Solar Surface Magnetism, ed. Rutten, R. J., & Schrijver, C. J. (Dordrecht: Kluwer), 303
- Martin, S. F., & McAllister, A. H. 1997, in Coronal Mass Ejections, ed. Crooker, N., Joselyn, J. A., & Feynman, J. (Washington: American Geophysical Union), 127

- Moore, R. L., & Roumeliotis, G. 1992, in Eruptive Solar Flares, ed. Svestka, Z., Jackson, B. V., & Machado, M. E. (New York: Springer-Verlag), 69
- Priest, E. R. 1988a, Dynamics and Structure of Quiescent Solar Prominences (Dordrecht: Kluwer)
- Priest, E. R. 1988b, ApJ, 328, 848
- Priest, E. R., Hood, A. W., & Anzer, U. 1989, ApJ, 344, 1010
- Priest, E. R., van Ballegooijen, A. A., & MacKay, D. H. 1996, ApJ, 460, 530
- Raadu, M. 1972, Sol. Phys., 22, 425
- Ridgway, C., & Priest, E. R. 1993, Sol. Phys., 146, 277
- Rust, D. M. 1994, Geophysical Research Letters, 21, 241
- Rust, D. M., & Kumar, A. 1994, Sol. Phys., 155, 69
- Rust, D. M., & Kumar, A. 1996, ApJ, 464, L199
- Ruzdjak, V., & Tandberg-Hanssen, E. 1990, Dynamics of Quiescent Prominences (New York: Springer-Verlag)
- Schmieder, B., Demoulin, P., Aulanier, G., & Golub, L. 1996, ApJ, 467, 881
- Steele, C. D. C., & Priest, E. R. 1989, Sol. Phys., 119, 157
- Sturrock, P. A. 1989, Sol. Phys., 121, 387
- Sturrock, P. A. 1992, in Eruptive Solar Flares, ed. Svestka, Z., Jackson, B. V., & Machado, M. E. (New York: Springer-Verlag), 397
- Tandberg-Hanssen, E. 1974, Solar Prominences (Dordrecht: Reidel)

- Tandberg-Hanssen, E. 1995, The Nature of Solar Prominences (Dordrecht: Kluwer)
- van Ballegooijen, A. A. 1999, in Magnetic Helicity in Space and Laboratory Plasmas, ed. Brown, M. R., Canfield, R. C., & Pevtsov, A. A. (Washington: American Geophysical Union), 213
- van Ballegooijen, A. A., & Martens, P. C. H. 1989, ApJ, 343, 971
- van Ballegooijen, A. A., & Martens, P. C. H. 1990, ApJ, 361, 283
- Vrsnak, B. 1990, Sol. Phys., 129, 295
- Vrsnak, B., Ruzdjak, V., Brajsa, R., & Dzubur, A. 1988, Sol. Phys., 116, 45
- Vrsnak, B., Ruzdjak, V., & Rompolt, B. 1991, Sol. Phys., 136, 151
- Webb, D., Rust, D., & Schmieder, B. 1998, New Perspectives on Solar Prominences (San Francisco: Astronomical Society of the Pacific)
- Xu, A.-A., & Wu, G. P. 1995, Sol. Phys., 159, 265
- Yang, W. H., Sturrock, P. A., & Antiochos, S. K. 1986, ApJ, 309, 383

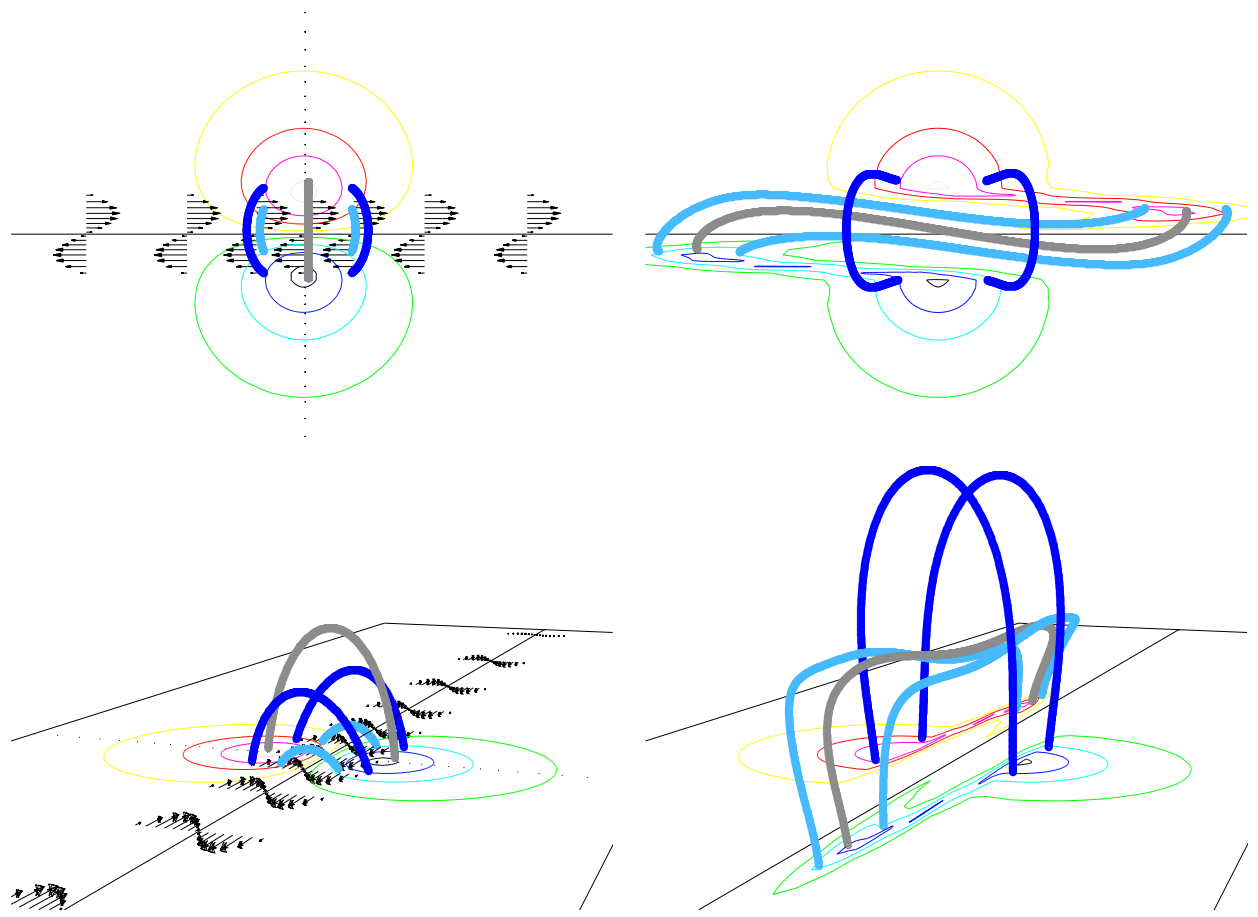


Plate 1. Overhead (upper panels) and perspective (lower panels) views of the initial conditions (left panels) and final results for modest footpoint displacements (right panels) of the prominence model are shown. Color contours on the bottom surface denote lines of constant B_z , while the thick loops denote selected magnetic field lines. The black arrows in the left panels show the direction and relative magnitudes of the imposed footpoint displacements. The configuration shown in the right panels may be compared with that of Antiochos, Dalhburg, & Klimchuk (1994).

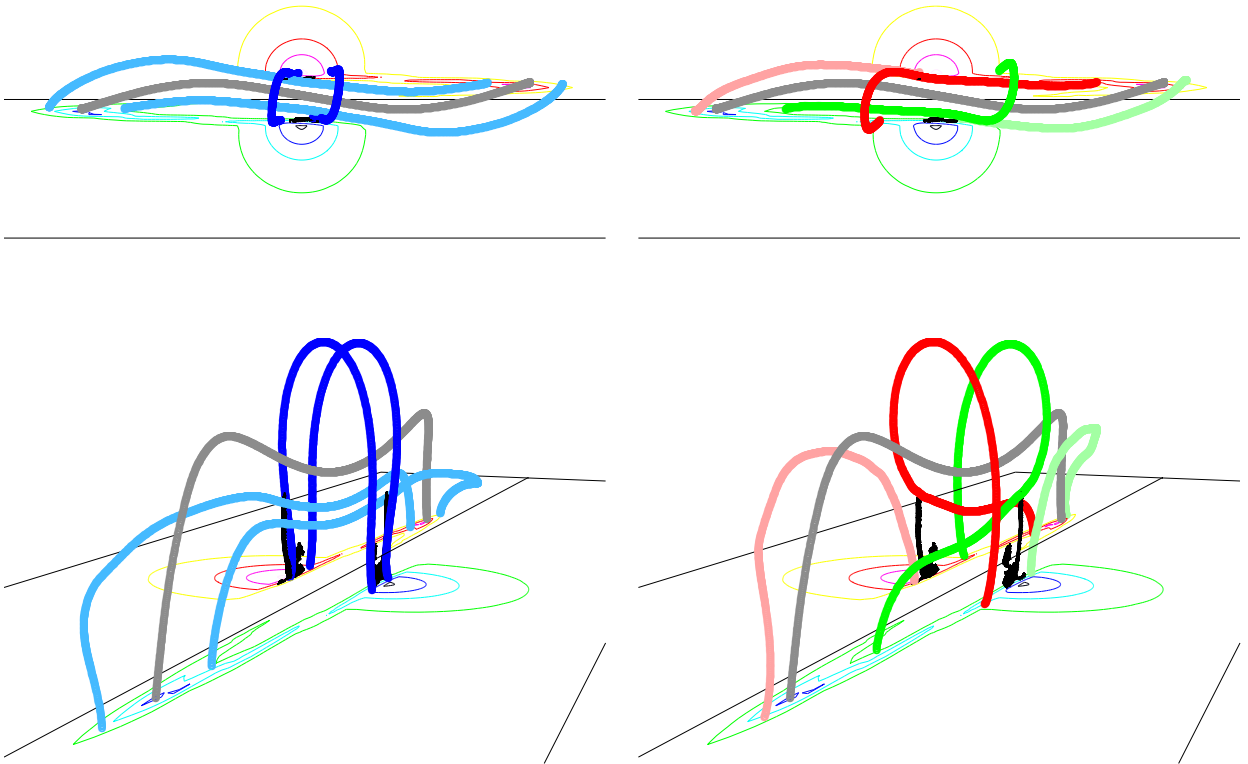


Plate 2. Views of two groups of field lines, at time $t = 55$ in the simulation, are shown. Pre-reconnection field is shown in dark and light blue in the left panels; post-reconnection field is shown in dark and light red and green in the right panels. The dark gray, dipped field line in the core of the prominence is common to all panels, as are the black isosurfaces of electric current density at 75% of maximum. This plate illustrates step one of the two-step reconnection process.

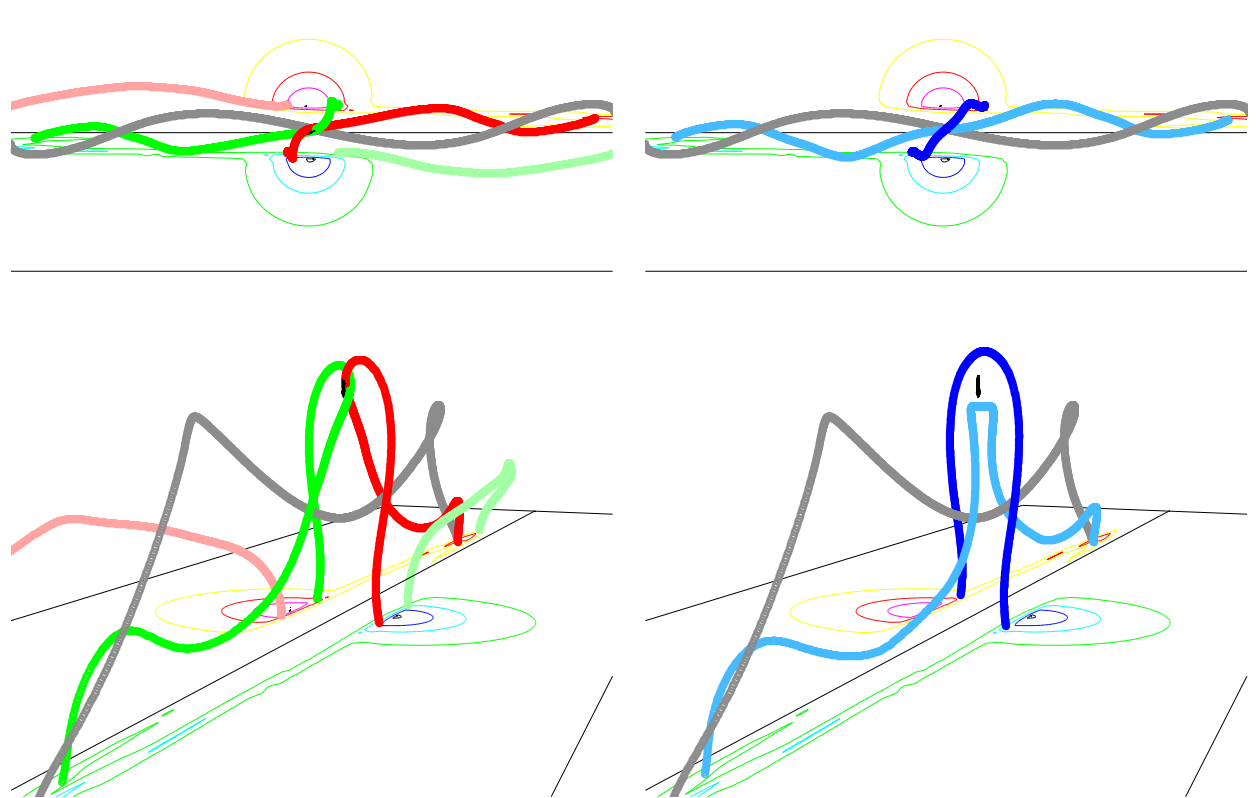


Plate 3. Views of another two groups of field lines, at time $t = 75$ in the simulation, are shown. Pre-reconnection field is shown in dark and light red and green in the left panels; post-reconnection field is shown in dark and light blue in the right panels. The pre-reconnection lines at the left are similar to lines produced earlier and shown at the right in Plate 2. The dark gray, dipped field line in the core of the prominence is common to all panels in this plate, as are the black isosurfaces of electric current density at 75% of maximum. This plate illustrates step two of the reconnection process.

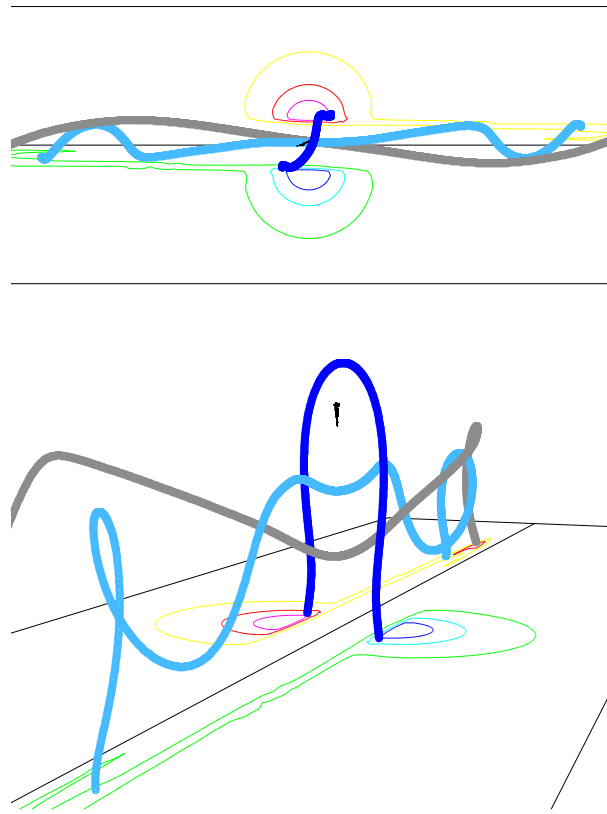


Plate 4. Views of a pair of post-reconnection field lines in dark and light blue, at time $t = 100$ in the simulation, are shown. These lines are similar to those displayed at the right in Plate 3. A dark gray, dipped field line in the core of the prominence is shown, as are black isosurfaces of electric current density at 90% of maximum.

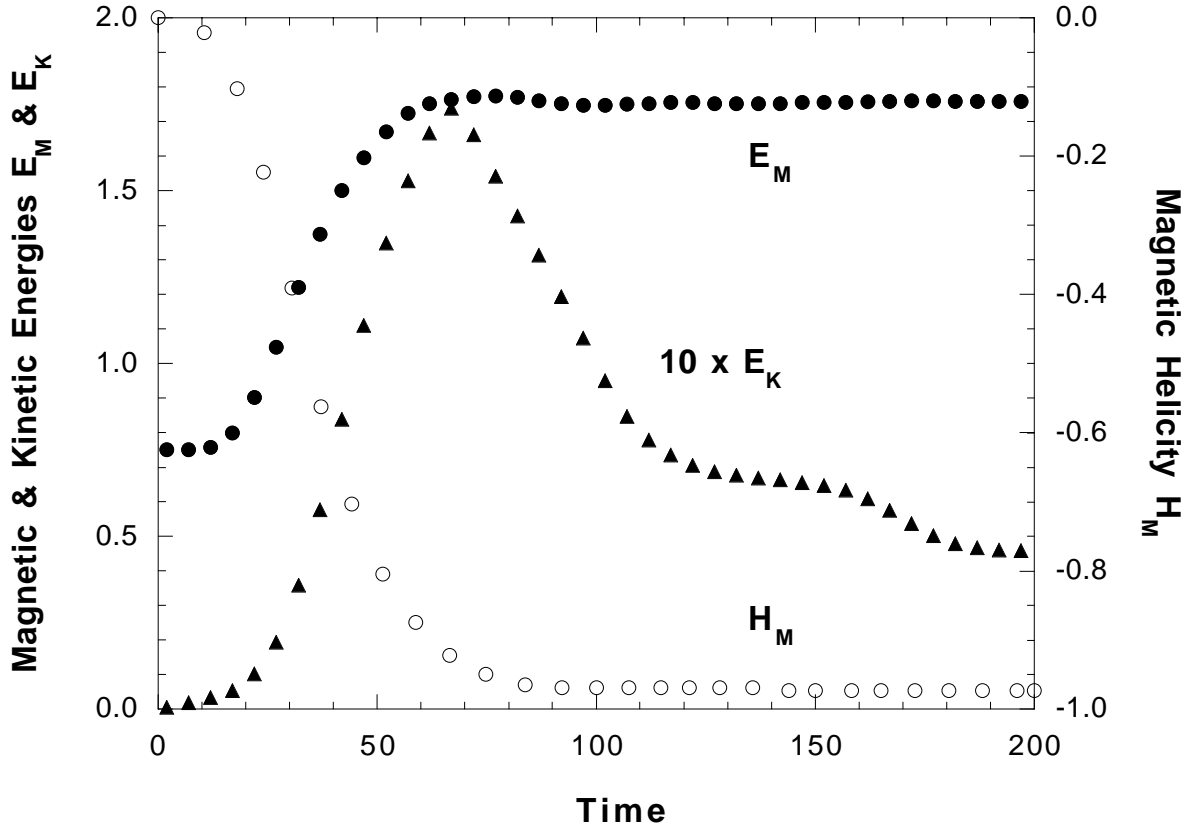


Fig. 1.— The magnetic and kinetic energies E_M and E_K (left axis, filled circles and filled triangles, respectively) and the magnetic helicity H_M (right axis, open circles) for the prominence simulation are displayed versus time t . The energies are normalized to $\bar{B}^2 d^3 / 8\pi = \Phi^2 / 32\pi L$ and the helicity to $\bar{B}^2 d^4 = \Phi^2 / 4$, where $\Phi = 2|\bar{B}|d^2$ is the magnetic flux in the bipole. Also, the kinetic energy has been scaled up by a factor of 10, for clarity.